ROYAL SOCIETY
OF CHEMISTRY

PAPER

Check for updates

Lattice strain and texture analysis of superhard $Mo_{0.9}W_{1.1}BC$ and $ReWC_{0.8}$ *via* diamond anvil cell deformation†

Marcus Parry, [a] Samantha Couper, [b] Aria Mansouri Tehrani, [c] Anton O. Oliynyk, [c] Jakoah Brgoch, [c] Lowell Miyagi [b] and Taylor D. Sparks [*a]

$Mo_{0.9}W_{1.1}BC$ and $ReWC_{0.8}$ compositions have recently been identified to have exceptional hardness and incompressibility. In this work, these compositions are analyzed *via in situ* radial X-ray diffraction experiments to comparatively assess lattice strain and texture development. Traditionally, Earth scientists have employed these experiments to enhance understanding of dynamic activity within the deep Earth. However, nonhydrostatic compression experiments provide insight into materials with exceptional mechanical properties, as they help elucidate correlations between structural, elastic, and mechanical properties. Here, analysis of differential strain (t/G) and lattice preferred orientation in $Mo_{0.9}W_{1.1}BC$ suggests that dislocation glide occurs along the (010) plane in orthorhombic $Mo_{0.9}W_{1.1}BC$. The (200) and (002) planes support the highest differential strain, while planes which bisect two or three axes, such as the (110) or (191), exhibit relatively lower differential strain. In $ReWC_{0.8}$, which crystallizes in a cubic NaCl-type structure, planar density is correlated to orientation-dependent lattice strain as the low-density (311) plane elastically supports more differential strain than the denser (111), (200), and (220) planes. Furthermore, results indicate that $ReWC_{0.8}$ likely supports a higher differential stress t than $Mo_{0.9}W_{1.1}BC$ and, based on a lack of texture development, bulk plastic yielding is not observed in $ReWC_{0.8}$ upon compression to $\sim$60 GPa.

Introduction

Superhard materials, classified by a Vickers hardness (H_V) exceeding 40 GPa, are utilized in a variety of applications including cutting, grinding, drilling, as well as in the automotive, aerospace, and defense industries.[1] Diamond ($H_V = 90$ GPa) is perhaps the most commonly recognized superhard material, consisting of a strong, dense network of short covalent bonds among tetrahedrally coordinated carbon atoms.[2–4] Other superhard materials combine light, main group elements to mimic the structure of diamond, such as cubic boron nitride (c-BN, $H_V = 55$ GPa) and BC_2N ($H_V = 65$ GPa).[5–7] Although these compounds have impressive mechanical properties, their synthesis is costly due to the extreme pressures required to achieve the desired structures.

More recently, research efforts have been directed towards another class of hard materials, transition metal (TM) borides

such as ReB_2 ($H_V = 45$ GPa) and WB_4 ($H_V = 43$ GPa).[8,9] The heavy transition metals are inherently incompressible due to their high density of valence electrons, while the light boron atoms maintain the propensity to form short directional covalent bonds. Materials in this class are of interest because of their synthetic accessibility, as common high temperature metallurgical techniques performed at ambient pressures are sufficient to achieve the desired structures. Furthermore, hardness of TM-borides can be enhanced through elemental substitution of the TM or through the formation of a second phase, optimizing valence electron count and atomic size effects. For instance, hardness of WB_4 is increased from $H_V = 43$ GPa to greater than 50 GPa (0.49 N indentation load) when doping to $W_{1-x}(TM)_xB_4$; $x = 8.0$ at% titanium, 8.0 at% zirconium, 6.0 at% hafnium, 3.0 at% molybdenum, 2.0 at% tantalum, 4.0 at% manganese, or 10.0 at% chromium.[10–12]

Our group recently developed a machine learning (ML) model to assist in the search for novel materials compositions with exceptional mechanical properties.[13] Specifically, a training set of density functional theory (DFT) calculated elastic constants was used to predict bulk (K) and shear (G) moduli of binary, ternary, and quaternary compounds compiled in Pearson's Crystal Database.[14] As G and K are intrinsic material properties correlated to hardness through Pugh's ratio ($G : K$), these predicted moduli were utilized as a proxy to identify potential superhard,

[a]Department of Materials Science and Engineering, University of Utah, Salt Lake City, Utah 84112, USA. E-mail: sparks@eng.utah.edu

[b]Department of Geology and Geophysics, University of Utah, Salt Lake City, Utah 84112, USA

[c]Department of Chemistry, University of Houston, Houston, Texas 77204, USA

† Electronic supplementary information (ESI) available. See DOI: 10.1039/c9ta06431a

ultraincompressible compositions, leading to the investigation of a ternary Re–W–C and quaternary Mo–W–B–C system.[13,15] Phase pure $ReWC_{0.8}$ and $Mo_{0.9}W_{1.1}BC$ were synthesized *via* common high temperature techniques and K_0 was assessed experimentally using near-hydrostatic high-pressure diamond anvil cell (DAC) diffraction, establishing a Birch–Murnaghan equation of state (EoS) up to pressures of ~30 GPa for $ReWC_{0.8}$ and ~50 GPa for $Mo_{0.9}W_{1.1}BC$. Experimental incompressibility was determined to be $K_0 = 380(8)$ GPa for $ReWC_{0.8}$ and $K_0 = 342(2)$ GPa for $Mo_{0.9}W_{1.1}BC$, corroborating the ML predictions within 10% and indicating that each composition is indeed ultraincompressible. In fact, both $ReWC_{0.8}$ and $Mo_{0.9}W_{1.1}BC$ demonstrated K_0 greater than that of WB_4 ($K_0 = 324(3)$ GPa) while also exhibiting hardness at the threshold of the superhard limit, as $H_V = 40(3)$ GPa for $ReWC_{0.8}$ and $H_V = 42(2)$ GPa for $Mo_{0.9}W_{1.1}BC$ (0.49 N load).[13,16]

While $ReWC_{0.8}$ and $Mo_{0.9}W_{1.1}BC$ exhibit promising hardness and bulk incompressibility, exploring anisotropic elastic and plastic deformation behavior can provide insights into the relationship between microstructure, elastic properties, and hardness. In radial diamond anvil cell (rDAC) diffraction experiments, a nonhydrostatic stress is imposed and lattice plane deformation behavior is observed *in situ*. Lattice planes deform elastically until the onset of plastic deformation, at which point they can no longer support the differential stress.[17] The imposed stress at the elastic–plastic transformation is inferred as the lower bound of the yield strength for the material. Furthermore, rDAC experiments are implemented to evaluate slip systems and observe the development of lattice preferred orientation, or texture, as a result of plastic deformation by dislocation glide.[18]

Deformation experiments in the rDAC have been primarily developed in the Earth sciences because understanding anisotropic lattice strain behavior and texture development in the materials of Earth's upper and lower mantle is necessary for the interpretation of seismic data.[17,19–26] Additionally, rDAC synchrotron diffraction has been used to explore deformation behavior and hardening mechanisms in hard, incompressible materials including OsB_2, $W_{1-x}(TM)_xB_4$ solid solutions, $W_{1-x}Ta_xB$ solid solutions, and $Zr_{1-x}Y_xB_{12}$ dodecaborides, though texture development is not reported.[27–32] In the present study, lattice strain and texture development are evaluated for $ReWC_{0.8}$ and $Mo_{0.9}W_{1.1}BC$ *via* rDAC axial compression experiments. Results are discussed in relation to the crystal structures of each compound, providing new insights into anisotropic deformation behavior.

Experimental

Phase pure $ReWC_{0.8}$ and $Mo_{0.9}W_{1.1}BC$ compositions were obtained *via* arc melting in a previous work.[13] The starting materials, Re (Alfa Aesar, 99.997%), W (Alfa Aesar, 99.5%), C (Sigma-Aldrich, ≥99.99%), Mo (Alfa Aesar, 99.95%), and crystalline B (Alfa Aesar, 99.5%), were weighed out in stoichiometric ratios to a total mass ≈ 0.4 g. The powders were pressed into pellets and arc melted using a current of 80 A and a water-cooled copper hearth under argon flow atmosphere until homogenous melting was achieved, flipping the ingot at least twice to ensure

mixing of the elements. The samples were ground to a fine powder with Diamonite mortar and pestle, mixing in 5% platinum powder as a pressure calibrant.[33] Solvent suspension in methanol was utilized to separate the finest particles from the bulk ground powder, and the solvent-separated fine powder was again ground to achieve even finer particle size. The mixtures were loaded into an X-ray transparent amorphous boron epoxy gasket housed in a Kapton confining ring.[34] As an additional pressure marker, a pellet of powdered ruby was added to each sample chamber.[35] Sample chambers were 50 μm in diameter and 50 μm thick.

Synchrotron experiments were carried out utilizing the facilities of the High Pressure Collaborative Access Team (HPCAT) at beamline sector 16-ID-B of the Advanced Photon Source (APS). Angle-dispersive X-ray diffraction spectra were collected in radial geometry using a MAR165 CCD detector and monochromatic X-rays ($\lambda = 0.4045$ Å for $Mo_{0.9}W_{1.1}BC$; $\lambda = 0.4049$ Å for $ReWC_{0.8}$). X-ray energy was ~30.5 keV and the beam was focused to 5 μm × 4 μm. A cerium dioxide standard was used to calibrate sample to detector distance (187.3 mm for $Mo_{0.9}W_{1.1}BC$ and 189.0 mm for $ReWC_{0.8}$), detector tilt, and detector rotation. A gas membrane and SYNTEK diamond anvil cell with 200 μm diameter flat culet diamond anvils were implemented to nonhydrostatically compress $ReWC_{0.8}$ and $Mo_{0.9}W_{1.1}BC$ to ~50 GPa in increments of 1–4 GPa at ambient temperature, collecting diffraction images at each step. The incident X-ray beam was perpendicular to the compression direction.

To monitor *in situ* development of texture and lattice strain during nonhydrostatic compression of $ReWC_{0.8}$ and $Mo_{0.9}W_{1.1}BC$ samples in an rDAC, Rietveld lattice strain and texture analysis of the synchrotron diffraction images was applied using the Materials Analysis Using Diffraction (MAUD) software package, as detailed by Wenk, *et al.* and briefly outlined below.[36,37] The 2D diffraction images were converted from polar coordinates to Cartesian coordinates using FIT2D and integrated in 5° sectors to generate 72 patterns.[38] Due to strong anisotropic stresses, the small integration step was necessary to capture texture of the samples.

Lattice strains, represented by $Q(hkl)$ factors, were calculated through the separate fitting of each diffraction peak based upon peak displacement and angle to the compression axis using the "Radial Diffraction in the DAC" model implemented in MAUD.[36,39,40] Under nonhydrostatic stress, measured d-spacings ($d_m(hkl)$) are dependent on the angle χ between the principle stress axis and the diffracting plane normal,

$$d_m(hkl) = d_p(hkl)[1 + (1 - 3\cos^2\chi)Q(hkl)], \quad (1)$$

where $d_p(hkl)$ is the d-spacing resulting from the hydrostatic component of pressure. The lattice strain $Q(hkl)$ is a function of shear moduli under Reuss isostress (G_R) and Voigt isostrain (G_V) approximations,

$$Q(hkl) = \frac{t}{3}\left[\frac{\alpha}{2G_R(hkl)} + \frac{1-\alpha}{2G_V}\right], \quad (2)$$

and $0 \le \alpha \le 1$.[41,42] The von Mises yield criterion states,

This journal is © The Royal Society of Chemistry 2019

J. Mater. Chem. A, 2019, **7**, 24012–24018 | **24013**

$$t = (\sigma_3 - \sigma_1) \leq 2\tau = \sigma_y, \tag{3}$$

where σ_3 is the maximum stress in the compression direction, σ_1 is the minimum stress parallel to the diamond culet, τ is the shear strength and σ_y is the yield strength. Thus, the axial stress component, or differential stress, t, gives a lower-bound estimate of the yield strength of the material. Furthermore, the differential stress of the sample can be estimated with the relation

$$t(hkl) = 6G(hkl)\langle Q(hkl)\rangle. \tag{4}$$

Because the experimental shear modulus and its pressure dependence are unknown for $ReWC_{0.8}$ and $Mo_{0.9}W_{1.1}BC$, the ratio of differential stress to shear modulus, $t(hkl)/G(hkl)$, is used as qualitative indicator for $t(hkl)$. The lattice strain parameter $Q(hkl)$ can be used to directly determine this ratio for each diffraction peak.

To refine texture, the Orientation Distribution Function (ODF) was determined *via* the Extended Williams, Imhof, Matthies, and Vinel (E-WIMV) algorithm, which is similar to the WIMV method but allows for incomplete and arbitrary pole figure coverage.[43] Pole figures were normalized to limit the potential introduction of texture artifacts.[37] Then, using Beartex, the ODF was smoothed with a 7.5° Gauss filter.[44] During axial compression, cylindrical symmetry about the compression axis is assumed and Inverse Pole Figures (IPFs) can be used to succinctly illustrate lattice preferred orientation of the samples in relation to the compression direction. Pole densities are expressed in multiples of random distribution (m.r.d.). An m.r.d. equal to 1 indicates a random distribution while perfect orientation in a single crystal corresponds to an m.r.d. of infinity.

Results and discussion

The development of lattice strain and crystallographic preferred orientation in $Mo_{0.9}W_{1.1}BC$ is assessed on compression at six distinct pressures of $P = 0.3, 7.0, 17.2, 26.4, 35.7,$ and 47.7 GPa, determined from the EoS for platinum.[33] During compression of $ReWC_{0.8}$, refinement of the platinum peaks proved difficult due to limited intensity and poor peak shape at higher pressures. Thus, corundum was used as the internal pressure standard for $ReWC_{0.8}$ samples.[35] Six spectra were analyzed on compression at $P = 4.1, 10.6, 20.3, 35.3, 47.4,$ and 61.0 GPa. Above $\sim$35 GPa, peak overlap and broadening likely reduce the accuracy of pressure determination compared to lower pressures. However, high pressure trends in texture and anisotropic lattice strain behavior can still be examined. Lattice parameters and associated error values for $Mo_{0.9}W_{1.1}BC$, $ReWC_{0.8}$, platinum, and corundum are available in the ESI Tables S1 and S2.†

Initial diffraction data for the $Mo_{0.9}W_{1.1}BC$ sample indicates a starting pressure of $P = 0.3$ GPa. Fig. 1a illustrates the collected diffraction data (bottom) and fit (top). No significant lattice strain is observed. Upon compression of the sample, diffraction peaks shift to larger Q-space values, attributable to a decrease in unit cell volume (Fig. 1b). Larger shifts in Q-space are observed in the direction of maximum stress, while smaller shifts are observed in regions perpendicular to the compression direction (parallel to the face of the diamond culets). The observed sinusoidal variability in peak position indicates lattice strain in the sample and intensity variations with azimuthal angle suggest potential texture development. The $ReWC_{0.8}$ diffraction data shows an initial pressure of $P = 4.1$ GPa as well as lattice strain in the sample pre-compression (Fig. 1c). As
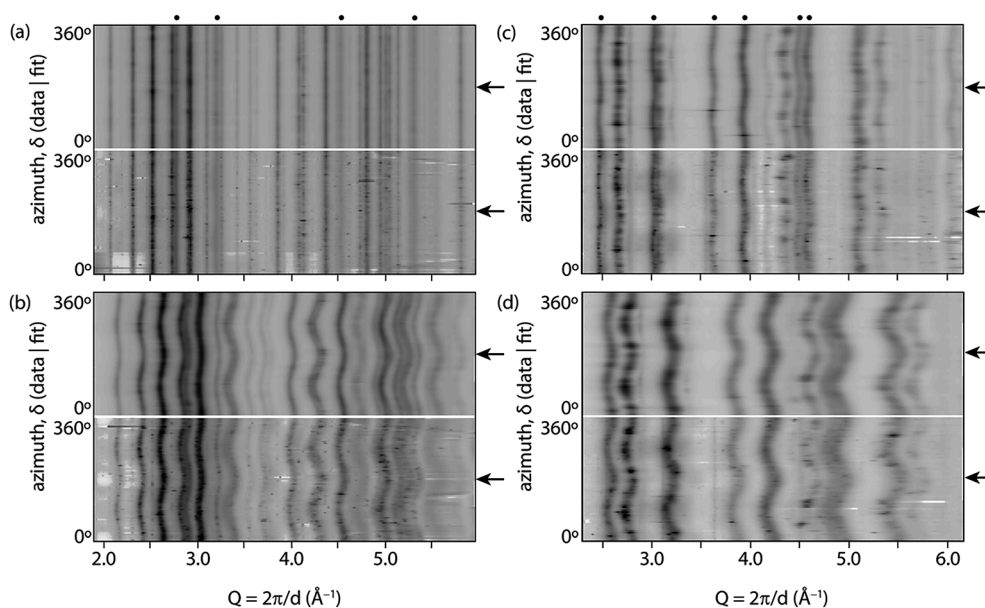

Fig. 1 Raw 2-D diffraction spectra (bottom) and Rietveld fit (top) for azimuth angles δ between 0° and 360° taken in 5° intervals. (a) $Mo_{0.9}W_{1.1}BC$ at $P = 0.3$ GPa; (b) $Mo_{0.9}W_{1.1}BC$ at $P = 7.0$ GPa; (c) $ReWC_{0.8}$ at $P = 4.1$ GPa; (d) $ReWC_{0.8}$ at $P = 35.3$ GPa. Arrows at the right of each plot indicate the compression direction. Peaks associated with the pressure calibrant are labeled above, while other peaks are associated with the main phase.

24014 | *J. Mater. Chem. A*, 2019, **7**, 24012–24018

This journal is © The Royal Society of Chemistry 2019

pressure is increased, diffraction peaks shift to a larger Q-space and lattice strain intensifies (Fig. 1d).

Prior to evaluating anisotropic lattice strain and texture development of $Mo_{0.9}W_{1.1}BC$ and $ReWC_{0.8}$ under axial compression, it is important to understand their crystal structures. $Mo_{0.9}W_{1.1}BC$ is orthorhombic ($Cmcm$) and is isostructural to the Mo_2BC parent phase. The crystal structure, depicted in Fig. 2a, is highly anisotropic. Boron atoms are bound together in zigzag chains extending in the [001] direction. These chains center the layers of face-sharing BTM_6 trigonal prisms, which alternate with carbon-rich planes comprised of face-sharing CTM_6 octahedra. The two crystallographically independent TM sites (Wyckoff 4c) are occupied by a statistical mixing of Mo and W. $ReWC_{0.8}$ adopts the cubic NaCl-type crystal structure ($Fm\bar{3}m$), as illustrated in Fig. 2b. Equivalent TM sites (Wyckoff 4a) are shared by Re and W atoms, while the carbon site (Wyckoff 4b) is deficient.

To explore the development of anisotropic lattice strain in $Mo_{0.9}W_{1.1}BC$ and $ReWC_{0.8}$, we consider the ratio of differential stress to shear modulus ($t(hkl)/G(hkl)$), equivalent to the differential strain, for each composition (Fig. 3). For $Mo_{0.9}W_{1.1}BC$, six well-defined hkl planes were selected from the X-ray patterns when evaluating lattice strain (Fig. 3a). We specifically chose the orthogonal (200) and (002) planes, as well as hkl planes bisecting the b-axis, to assess directional-dependent deformation behavior of the crystal structure under nonhydrostatic compression. Unfortunately, reflections orthogonal to the b-axis within the refinement range were either indistinguishable from other hkl planes or low in intensity, so lattice strain could not be refined. Refined $Q(hkl)$ values are provided in ESI Tables S3 and S4† for the lattice planes of interest.

As shown in Fig. 3a, the differential strain supported by each lattice plane generally increases as the sample is axially compressed. At the highest pressure of $P = 47.7$ GPa, the (200)
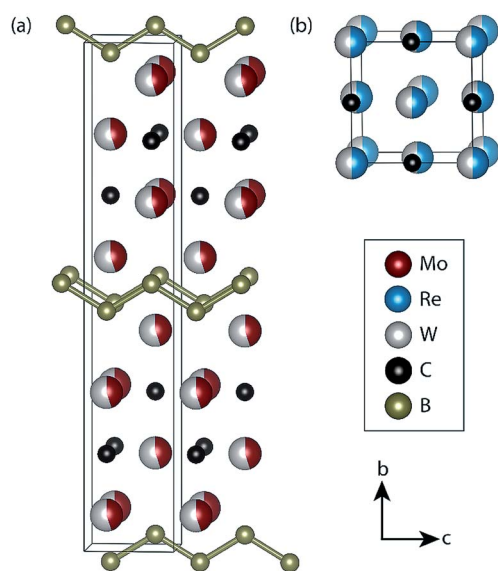

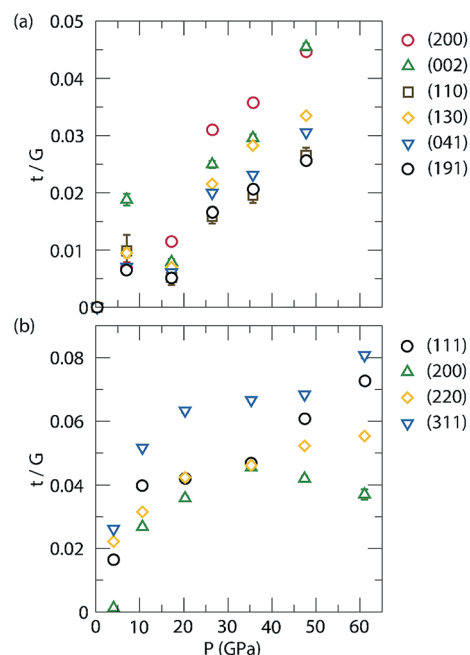**Fig. 3** Development of differential strain, $t(hkl)/G(hkl)$, as a function of pressure for (a) six lattice planes in orthorhombic $Mo_{0.9}W_{1.1}BC$ and (b) four lattice planes in cubic $ReWC_{0.8}$. Error bars are shown when larger than the marker size.

Fig. 2 Crystal structures of (a) $Mo_{0.9}W_{1.1}BC$ and (b) $ReWC_x$ where $x = 2$.

and (002) lattice planes exhibit the greatest differential strain of 4.5%. The (200) and (002) planes in $Mo_{0.9}W_{1.1}BC$ are parallel to the long b-axis and are therefore orthogonal to the layers of zigzag boron chains. These covalent chains likely provide the additional elastic support to achieve the high $t(hkl)/G(hkl)$ ratios and, as a result, these planes are less prone to slip. On the contrary, $t(191)/G(191)$ is equal to 2.6% at the same pressure, elastically supporting the least differential strain. Other planes analyzed, including the (110), (130), and (041), support a lattice strain between 2.6% and 3.3%. Although reflections orthogonal to the b-axis were not analyzed directly, we speculate that these planes support similar or less differential strain than the (191) plane due to the lack of covalent support.

The development of orientation-dependent differential strain in $ReWC_{0.8}$ is illustrated in Fig. 3b. Above $P = 10$ to 15 GPa, differential strain on (311) and (200) appear to plateau while strain on (111) and (220) continue to increase. The (200) plane elastically supports the least differential strain with a maximum $t(hkl)/G(hkl)$ ratio of 4.6% at $P = 35.3$ GPa which dwindles to 3.7% as pressure is increased to $P = 61.0$ GPa. The (111) and (220) planes support similar differential strain of 4.7% and 4.6% respectively at $P = 35.3$ GPa. Contrarily, the differential stress to shear ratio for the (311) plane is equal to 6.6%, elastically supporting the most differential strain. In the $ReWC_{0.8}$ crystal structure, the (311) plane has a lower planar density compared to the (200), (111), and (220) planes, resulting in its ability to support differential strain and a lower tendency to slip. In direct contrast to these findings, a recent high-pressure study examining NaCl-type ($Fm\bar{3}m$) metal dodeca-borides ZrB_{12}, YB_{12}, and $Zr_{0.5}Y_{0.5}B_{12}$ found the (200) plane to

support the most differential strain while the (111) supported the least, suggestive of a (111) slip system.[32] In these metal dodecaborides, each metal atom centers a cuboctahedral cluster formed by 24 boron atoms. The cuboctahedron cages of covalently bound boron atoms are likely the root of the observed differences in slip systems and plastic properties when compared to the carbide examined here, $ReWC_{0.8}$.

Interestingly, although previously reported Vickers hardness of $ReWC_{0.8}$ and $Mo_{0.9}W_{1.1}BC$ are similar, observed differential strain in $ReWC_{0.8}$ is much greater than that of $Mo_{0.9}W_{1.1}BC$.[13] As noted above, $t(hkl)/G(hkl)$ for $ReWC_{0.8}$ is in the range of 4.6% to 6.7% at $P \sim 35$ GPa while $Mo_{0.9}W_{1.1}BC$ exhibits a much lower range from 2.0% to 3.6%. This implies that either $G(hkl)$ of $ReWC_{0.8}$ is significantly lower than that of $Mo_{0.9}W_{1.1}BC$ or differential stress is much greater. In our previous work, shear moduli predicted *via* machine learning suggest statistically similar G values for each composition ($G = 192$ GPa for $Mo_{0.9}W_{1.1}BC$ and $G = 182$ GPa for $ReWC_x$ where $x = 2$; root-mean-square error = 16.5 GPa).[13] Assuming shear moduli are in fact similar, $t(hkl)$ must be significantly larger in $ReWC_{0.8}$ than $Mo_{0.9}W_{1.1}BC$ and it is possible that these materials have considerably different pressure dependence of elastic and plastic properties.

To evaluate the development of lattice preferred orientation in $Mo_{0.9}W_{1.1}BC$, IPFs of the compression direction are presented in Fig. 4. At low pressure, $P = 0.3$ GPa, the sample is

essentially random with a maximum m.r.d. of 1.16. Development of (010) texture occurs upon compression to $P = 7.0$ GPa, with a m.r.d. of 1.99. Texture saturation appears to occur, as the (010) texture is sustained through a pressure of $P = 47.7$ GPa with a m.r.d. of 1.66. This indicates that the (010) plane, or *b*-axis, orients at high angles to the compression axis. Previous plasticity modeling of texture development during axial compression shows that for the orthorhombic (*Cmcm*) structure, the development of a (010) maximum in the compression direction is due to slip on the (010) plane in either the [100] or $\langle 101 \rangle$ directions.[23] This plane is parallel to the boron chains in the structure and it is thus unsurprising that glide occurs on a plane that does not require breaking of the B–B bonds.

Fig. 5 depicts texture development in $ReWC_{0.8}$. Throughout compression, texture remains essentially random. The range of m.r.d. values observed across all IPFs is narrow with maximum values of 1.22, 1.20, 1.22, 1.28, 1.19, and 1.06 at $P = 4.1$, 10.6, 20.3, 35.3, 47.4, and 61.0 GPa, respectively. Thus, it is unlikely that bulk plastic yielding has occurred in this sample. In relation to trends observed Fig. 3b, dislocation glide generally results in anisotropic relaxation of differential strain which would be consistent with the observed anisotropic behavior of $t(hkl)/G(hkl)$ on the various lattice planes. A previous examination into the plastic deformation behavior of periclase ($Fm\bar{3}m$) reveals a maxima in $Q(200)$ attributed to dislocation pinning, which subsides after initial yielding and relaxation of deviatoric
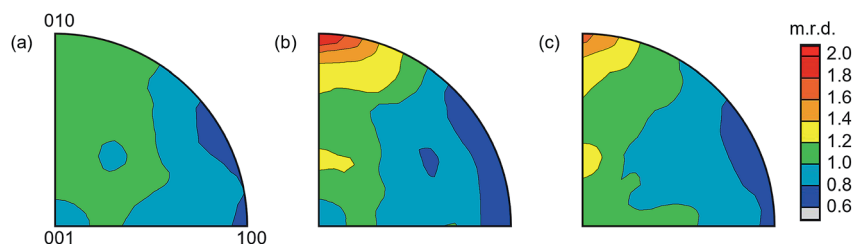

Fig. 4 Inverse pole figures of the compression direction representing texture evolution in $Mo_{0.9}W_{1.1}BC$ at (a) 0.3 GPa, (b) 7.0 GPa, and (c) 47.7 GPa. Equal area projection, linear contours are expressed in multiples of random distribution (m.r.d.).
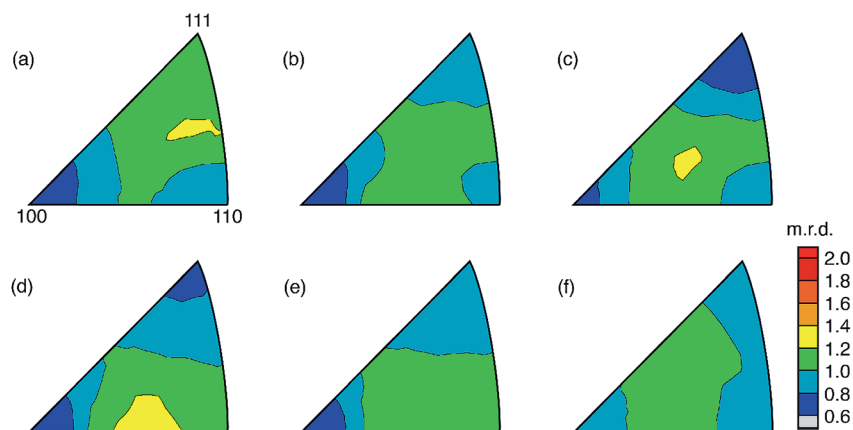

Fig. 5 Inverse pole figures (equal area projection) of the compression direction representing texture evolution in $ReWC_{0.8}$ at (a) 4.1 GPa, (b) 10.6 GPa, (c) 20.3 GPa, (d) 35.3 GPa, (e) 47.4 GPa, and (f) 61.0 GPa. Equal area projection, linear contours are expressed in multiples of random distribution (m.r.d.).

strains.[22] This behavior is consistent with observed trends in $t(hkl)/G(hkl)$ for $ReWC_{0.8}$ and suggests potential slip on the (110) plane. However, the lack of texture evolution does not appear to support significant activity of dislocation glide, though it is possible that the sluggish development of texture is occurring.

Yielding by slide along grain boundaries could result in a plateau in differential strain without the development of significant texture but would not result in anisotropic relaxation of differential strain. Furthermore, grain boundary sliding is likely to be suppressed at high confining pressure due to large normal stresses at grain boundary contacts. Another possibility is that the plateau in $t(hkl)/G(hkl)$ of (311) and (200) planes is due to changes in elastic properties with pressure. In our previous work, while determining the Birch–Murnaghan EoS for $ReWC_{0.8}$, a kink was observed in the V/V_0 compression curve above $P = 30$ GPa.[13] The observed plateau in $t(hkl)/G(hkl)$ data for each plane appears to be centered around $P = 30$ GPa, and it is possible that these phenomena are related. The origin of these events may be due to an isostructural phase transition or a rapid change in elastic properties at high pressure, both of which can cause anisotropic relaxation of differential strain.

Conclusions

In this study, nonhydrostatic high-pressure diffraction studies were performed in the rDAC to assess anisotropic lattice strain and texture development of $ReWC_{0.8}$ and $Mo_{0.9}W_{1.1}BC$. In orthorhombic $Mo_{0.9}W_{1.1}BC$, the (002) and (200) planes parallel to the long b-axis support the greatest differential strain. These planes are orthogonal to covalently bonded chains of boron, decreasing their susceptibility to slip. Conversely, lattice planes bisecting the b-axis demonstrate lower $t(hkl)/G(hkl)$ ratios. Texture analyses show that the (010) planes orient at high angles to the compression direction, indicative of slip along this plane. Orientation-dependent lattice strain analyses of cubic $ReWC_{0.8}$ suggest higher differential strain than observed for $Mo_{0.9}W_{1.1}BC$, suggesting differential stress t is greater in $ReWC_{0.8}$ than $Mo_{0.9}W_{1.1}BC$. In $ReWC_{0.8}$, the (111), (200), and (220) planes elastically support less differential strain than the less dense (311) plane. Texture analyses did not reveal the development of lattice preferred orientation upon compression, implying that bulk plastic yielding may not have occurred. By examining anisotropic deformation behavior of $Mo_{0.9}W_{1.1}BC$ and $ReWC_{0.8}$, we have gathered new insights regarding deformation mechanisms and correlations among structural, elastic, and mechanical properties. Findings will benefit future design of synthetically accessible materials with superior mechanical properties.

Conflicts of interest

There are no conflicts of interest to declare.

Acknowledgements

References

1 R. B. Kaner, J. J. Gilman and S. H. Tolbert, *Science*, 2005, **308**, 1268–1269.

2 J. Haines, J. M. Léger and G. Bocquillon, *Annu. Rev. Mater. Sci.*, 2001, **31**, 1–23.

3 F. P. Bundy, H. T. Hall, H. M. Strong and R. H. Wentorf Jr, *Nature*, 1955, **176**, 51–55.

4 R. H. Wentorf, R. C. Devries and F. P. Bundy, *Science*, 1980, **208**, 873–880.

5 B. P. Singh, V. L. Solozhenko and G. Will, *Diamond Relat. Mater.*, 1995, **4**, 1193–1195.

6 V. L. Solozhenko, S. N. Dub and N. V. Novikov, *Diamond Relat. Mater.*, 2001, **10**, 2228–2231.

7 R. H. Wentorf, *J. Chem. Phys.*, 1961, **34**, 809–812.

8 H.-Y. Chung, M. B. Weinberger, J. B. Levine, R. W. Cumberland, A. Kavner, J.-M. Yang, S. H. Tolbert and R. B. Kaner, *Science*, 2007, **316**, 436–439.

9 R. Mohammadi, A. T. Lech, M. Xie, B. E. Weaver, M. T. Yeung, S. H. Tolbert and R. B. Kaner, *Proc. Natl. Acad. Sci. U. S. A.*, 2011, 10958–10962.

10 G. Akopov, M. T. Yeung, C. L. Turner, R. Mohammadi and R. B. Kaner, *J. Am. Chem. Soc.*, 2016, **138**, 5714–5721.

11 R. Mohammadi, M. Xie, A. T. Lech, C. L. Turner, A. Kavner, S. H. Tolbert and R. B. Kaner, *J. Am. Chem. Soc.*, 2012, **134**, 20660–20668.

12 R. Mohammadi, C. L. Turner, M. Xie, M. T. Yeung, A. T. Lech, S. H. Tolbert and R. B. Kaner, *Chem. Mater.*, 2016, **28**, 632–637.

13 A. Mansouri Tehrani, A. O. Oliynyk, M. Parry, Z. Rizvi, S. Couper, F. Lin, L. Miyagi, T. D. Sparks and J. Brgoch, *J. Am. Chem. Soc.*, 2018, **140**, 9844–9853.

14 P. Villars and K. Cenzual, *Pearson's Crystal Data: Crystal Structure Database for Inorganic Compounds*, 2014.

15 X.-Q. Chen, H. Niu, D. Li and Y. Li, *Intermetallics*, 2011, **19**, 1275–1281.

16 M. Xie, R. Mohammadi, Z. Mao, M. M. Armentrout, A. Kavner, R. B. Kaner and S. H. Tolbert, *Phys. Rev. B: Condens. Matter Mater. Phys.*, 2012, **85**, 064118.

17 S. Merkel, *J. Phys.: Condens. Matter*, 2006, **18**, S949–S962.

This journal is © The Royal Society of Chemistry 2019

J. Mater. Chem. A, 2019, **7**, 24012–24018 | **24017**

18 H.-R. Wenk, I. Lonardelli, S. Merkel, L. Miyagi, J. Pehl, S. Speziale and C. E. Tommaseo, *J. Phys.: Condens. Matter*, 2006, **18**, S933–S947.

19 L. Haozhe, H.-R. Wenk and T. S. Duffy, *J. Phys.: Condens. Matter*, 2006, **18**(25), DOI: 10.1088/0953-8984/18/25/E01.

20 L. Miyagi, S. Merkel, T. Yagi, N. Sata, Y. Ohishi and H.-R. Wenk, *Phys. Earth Planet. Inter.*, 2009, **174**, 159–164.

21 S. Merkel, H.-R. Wenk, J. Shu, G. Shen, P. Gillet, H. K. Mao and R. J. Hemley, *J. Geophys. Res.: Solid Earth*, 2002, **107**, ECV 3-1–ECV 3-17.

22 F. Lin, N. Hilairet, P. Raterron, A. Addad, J. Immoor, H. Marquardt, C. N. Tomé, L. Miyagi and S. Merkel, *J. Appl. Phys.*, 2017, **122**, 205902.

23 L. Miyagi, N. Nishiyama, Y. Wang, A. Kubo, D. V. West, R. J. Cava, T. S. Duffy and H.-R. Wenk, *Earth Planet. Sci. Lett.*, 2008, **268**, 515–525.

24 D. J. Barber, H.-R. Wenk, J. Gomez-Barreiro, E. Rybacki and G. Dresen, *Phys. Chem. Miner.*, 2007, **34**, 73–84.

25 S. Zhang, S.-I. Karato, J. Fitz Gerald, U. H. Faul and Y. Zhou, *Tectonophysics*, 2000, **316**, 133–152.

26 H.-R. Wenk, E. Rybacki, G. Dresen, I. Lonardelli, N. Barton, H. Franz and G. Gonzalez, *Phys. Chem. Miner.*, 2006, **33**, 667–676.

27 H.-Y. Chung, J. M. Yang, S. H. Tolbert and R. B. Kaner, *J. Mater. Res.*, 2008, **23**, 1797–1801.

28 J. Lei, M. T. Yeung, R. Mohammadi, C. L. Turner, J. Yan, R. B. Kaner and S. H. Tolbert, *J. Appl. Phys.*, 2019, **125**, 082529.

29 M. Xie, R. Mohammadi, C. L. Turner, R. B. Kaner, A. Kavner and S. H. Tolbert, *Phys. Rev. B: Condens. Matter Mater. Phys.*, 2014, **90**, 104104.

30 M. Xie, R. Mohammadi, C. L. Turner, R. B. Kaner, A. Kavner and S. H. Tolbert, *Appl. Phys. Lett.*, 2015, **107**, 041903.

31 H. Dong, S. Dorfman, Y. Chen, H. Wang, J. Wang, J. Qin, D. He and T. Duffy, *J. Appl. Phys.*, 2012, **111**, 123514.

32 J. Lei, G. Akopov, M. T. Yeung, J. Yan, R. B. Kaner and S. H. Tolbert, *Adv. Funct. Mater.*, 2019, **29**, 1900293.

33 Y. Fei, A. Ricolleau, M. Frank, K. Mibe, G. Shen and V. Prakapenka, *Proc. Natl. Acad. Sci. U. S. A.*, 2007, **104**, 9182–9186.

34 S. Merkel and T. Yagi, *Rev. Sci. Instrum.*, 2005, **76**, 046109.

35 L. S. Dubrovinsky, S. K. Saxena and P. Lazor, *Phys. Chem. Miner.*, 1998, **25**, 434–441.

36 H.-R. Wenk, P. Kaercher, W. Kanitpanyacharoen, R. Vasin, L. Lutterotti and L. Miyagi, *Powder Diffr.*, 2014, **29**, 220–232.

37 L. Lutterotti, M. Bortolotti, G. Ischia, I. Lonardelli and H.-R. Wenk, *Z. Kristallogr.*, 2007, **26**, 125–130.

38 A. P. Hammersley, *J. Appl. Crystallogr.*, 2016, **49**, 646–652.

39 A. K. Singh, *J. Appl. Phys.*, 1993, **73**, 4278–4286.

40 A. K. Singh, C. Balasingh, H.-K. Mao, R. J. Hemley and J. Shu, *J. Appl. Phys.*, 1998, **83**, 7567–7575.

41 A. Reuss, *J. Appl. Math. Mech.*, 1929, **9**, 49–58.

42 W. Voigt, *Lehrbuch der kristallphysik : (mit ausschluss der kristalloptik)*, 1928.

43 S. Matthies and G. W. Vinel, *Phys. Status Solidi B*, 1982, **112**, K111–K114.

44 H.-R. Wenk, S. Matthies, J. Donovan and D. Chateigner, *J. Appl. Crystallogr.*, 1998, **31**, 262–269.